Int. J. Electrochem. Sci., 10 **(2015)** 3693 - 3706

International Journal of
ELECTROCHEMICAL
SCIENCE
www.electrochemsci.org

Morphology-dependent Performance of Nanostructured MnO_2 as an Oxygen Reduction Catalyst in Microbial Fuel Cells

Haoran Yuan[1, 2], *Lifang Deng*[1,2,*], *Yujie Qi*[1, 2], *Noriyuki Kobayashi*[3], *Masanobu Hasatani* [3]

[1] Guangzhou Institute of Energy Conversion Chinese Academy of Sciences, Guangzhou 510640, China
[2] Key Laboratory of Renewable Energy Chinese Academy of Sciences, Guangzhou 510640, China
[3] EcoTopia Science Institute, Nagoya University, Nagoya 464-8603, Japan
[*]E-mail: denglf@ms.giec.ac.cn

Received: 10 December 2014 / *Accepted:* 12 February 2015 / *Published:* 23 March 2015

Different nanostructures (nanoflowers, nanorods and nanotubes) of manganese dioxide (MnO_2) were successfully synthesized using hydrothermal methods with different dwell times and were demonstrated to be efficient and stable cathode catalysts for the oxygen reduction reaction (ORR). Subsequent examination of these nanostructures using field-emission scanning electron microscopy and transmission electron microscopy revealed a strong correlation between the dwell time and the resulting morphology of the nanostructures and confirmed the successful synthesis of nanotubes. The electrocatalytic activities of the different nanostructures were investigated using cyclic voltammetry and linear sweep voltammetry, and the results indicated that all of the MnO_2 nanostructures can catalyze the ORR with different catalytic activities. The nanotubes appeared to possess the highest catalytic activity, with a more positive peak potential and a larger ORR peak current. Additionally, a maximum power density of 11.6 W/m^3 was produced by the microbial fuel cell (MFC) with the nanotube cathode, which was higher than that of the other nanostructures and comparable to that of Pt/C (14.1 W/m^3). The results of this study demonstrate that nanotubes are ideal crystal structures for MnO_2 and that they offer a good alternative to Pt/C for practical MFC applications.

Keywords: Hydrothermal; Nanostructured manganese dioxide; Electrochemical oxygen-reduction activity; Cathode catalyst; Microbial fuel cell

1. INTRODUCTION

Microbial fuel cells (MFCs), which are one of the most promising methods for enhancing water and waste treatment, have attracted substantial interest for wastewater treatment in recent years [1-4]. However, their small-scale power output and high cost have limited the application of MFCs in this real field. The cathode has been reported to be one of the key components of MFCs with potential for

improvement to achieve a higher power output due to the slow reaction kinetics of the oxygen reduction reaction (ORR) [5-7]. Platinum (Pt)-based catalysts are commonly used to improve the performance of the ORR because of their high efficiency. Unfortunately, the high price and limited availability of Pt limit the further scaling up of MFCs. Therefore, considerable research efforts have been focused on non-precious metal catalysts as alternatives to Pt in fuel cells.

As an important functional metal oxide, nanostructured manganese dioxide (MnO_2) exhibits fast electrokinetics and excellent catalytic activity due to its high surface area and large number of active sites. The lower toxicity, abundance, low cost, redox stability, catalytic activity and environmentally benign nature of MnO_2 nanocatalysts have increased their potential applications in fields such as ion batteries [8], supercapacitors [9-12], magnetic materials [13], and MFC catalysts [14-17]. MnO_2 exists in several kinds of crystallographic forms (such as α, β, γ, δ, and so on). In 2009, Zhang et al. [18] reported that β-MnO_2 possessed the potential to improve the feasibility of scaling-up MFCs for real applications. In contrast, Kalubarme et al. [19] suggested that the excellent ORR activity of α-MnO_2 over the β and δ phases is attributed to the specific engineering of its crystal structure and to its high catalytic activity. In addition to the crystal structure, other factors, such as size, morphology, and surface area, influence the ORR activities of MnO_2 materials. For example, Liu et al. [20] demonstrated that nanostructured MnO_x prepared using an electrochemical deposition method was an effective ORR catalyst in an MFC, generating a peak electrical power density of 772.8 mW/m^3. Li et al. [21, 22] investigated manganese oxides with a cryptomelane-type octahedral molecular sieve (OMS-2) structure and found that they were comparable to Pt. Truoung et al. [23] reported that MnO_2 nanotubes exhibited higher surface areas exposed to the surrounding electrolyte, which may favor charge-transfer reactions. Yuan et al. [16] compared the performance of the hydrothermally synthesized MnO_2 (HSM) with the naturally synthesized MnO_2 (NSM), and found that HSM exhibited more positive. However, there have been no systematic studies on synthesizing MnO_2 with different crystal structures and morphologies as ORR catalysts for MFCs, and the mechanisms for the formation of different morphologies of MnO_2 have not yet been fully elucidated.

In this study, various MnO_2 nanostructures were synthesized using an optimized hydrothermal route under mild conditions. The nanostructures were changed through simple adjustments to the hydrothermal dwell time, and the prepared materials were tested as cathode catalysts in MFCs to evaluate their electrochemical properties. The results of this study will provide reference data for applying the proposed synthetic process in environmental technology.

2. EXPERIMENTAL

2.1 Synthetic procedure

Hydrated manganese sulfate ($MnSO_4 \cdot H_2O$) and potassium permanganate ($KMnO_4$) were supplied by the Guangzhou Chemical Reagent Factory (Guangdong, China). All of the chemicals were of analytical grade and were used as received without further purification. Distilled water was used in all of syntheses.

Nanostructured MnO_2 was prepared via the hydrothermal treatment of $MnSO_4 \cdot H_2O$ and $KMnO_4$ solutions [24]. Specifically, 0.2 g of $MnSO_4 \cdot H_2O$ and 0.5 g of $KMnO_4$ were dissolved in 100 mL of distilled water. The well-mixed aqueous solution of $KMnO_4$ and $MnSO_4$ was transferred to a Teflon-lined pressure vessel (Qiangqiang Instrument, Shanghai, China) and then loaded into an oven preheated to 140°C. The dwell time for the reaction was adjusted from 2 h to 18 h in 2-h intervals to optimize the electrochemical properties of the synthesized materials for use in MFCs (the obtained materials were named samples I to IX).

After the reaction reached completion, the pressure vessel was naturally cooled to room temperature. The MnO_2 precipitate that formed was filtered, washed with distilled water until the pH of the wash water was neutral (pH 7.0), and finally dried at 100°C in air.

2.2 Morphological and structural characterization

The particle morphology and structure of the prepared MnO_2 were characterized using field-emission scanning electron microscopy (FE-SEM, Model S-4800, Hitachi Ltd., Tokyo, Japan) and high-resolution transmission electron microscopy (HR-TEM, Model 2010, JEOL Ltd., Tokyo, Japan). The specific surface area of MnO_2 was measured using the Brunauer-Emmett-Teller (BET) method, in which the adsorption of nitrogen (N_2) at 77 K was measured using a sorptometer (Model 1800, Carlo Erba Instruments, Italy).

The crystal structure of the prepared MnO_2 was determined using an X-ray power diffractometer (XRD, Model X'Pert-PRO, PANalytical Corp., Almelo, The Netherlands) with a Cu Kα target ($\lambda = 0.154056$ nm). The diffractometer was operated using a tube voltage and current of 40 kV and 40 mA, respectively. Diffraction data were recorded from 5° to 80° 2θ with a step size of 0.02° 2θ and a count time of 1 s per step (θ accuracy = ±0.002°).

2.3 Electrochemical measurement

Cyclic voltammetry (CV) measurements were conducted using a potentiostat (Model PGSTAT 30, Autolab, Utrecht, The Netherlands) with a three-electrode system (Ecochemie, Utrecht, The Netherlands). A 3-mm-diameter glassy carbon electrode coated with the catalyst served as the working electrode, a platinum (Pt) wire served as the counter electrode, and silver/silver chloride was used as the reference electrode (Ag/AgCl, [saturated KCl], 222 mV vs. standard hydrogen electrode). The CV measurements were performed from –0.6 to 0.2 V at a scan rate of 100 mV/S in an aqueous electrolyte system (0.l M KOH). Prior to each scan series, the electrolyte solution was bubbled with O_2 (or N_2) for 30 min to establish an aerobic (or anaerobic) environment, with a 3-min time gap between every two scans.

Furthermore, the electrochemical oxygen reduction reaction (ORR) activities of the samples were studied using linear sweep voltammetry in a 0.1 M KOH aqueous electrolyte with a rotating-disc electrode (RDE, rotation rate 300–1200 rpm, and scan rate 10 mV/s). For comparison, commercial Pt/C (30 wt% platinum on carbon) was tested following the same procedure.

2.4 MFC configuration and operation

The as-synthesized MnO_2 powders were employed as cathode catalysts for single-chamber air-cathode MFCs. As-synthesized MnO_2, Ketjenblack (conductive material), and polyvinylidene fluorine (binder) were mixed with a weight ratio of 65:20:15 in 1 mL of N-methyl-2-pyrrolidone. After being dispersed by ultrasonicating for 30 min, the mixture was coated on the surface of the cathode carbon cloth. The fabrication of the laboratory MFCs and the compositions of the electrolytes and anode electrodes were similar to those presented in our previous work [25].

Carbon felt (5 cm × 5 cm × 0.5 cm, Panex 33160K, Zoltex, St. Louis, MO, USA) was used as the anode. Carbon cloth and a cation-exchange membrane were hot-pressed together to create the cathode. A titanium wire was inserted into the carbon felt and carbon cloth to connect the circuit. The air-cathode MFC consisted of a plastic (Plexiglas) cuboid chamber (2 cm × 5 cm × 5 cm), and the anode chamber of the MFC was filled with 40 mL of leachate collected during the biodrying (i.e., the pretreatment) of municipal solid waste from a Boluo waste treatment plant. All of the MFC reactors were inoculated with mixed-culture biofilms obtained from another MFC that was initially inoculated with leachate and that had been operating for more than four months. I–V polarization curves were obtained by varying the external resistance from 50 to 10000 Ω when the voltage output approached a steady state, and the individual electrode potentials were measured versus the Ag/AgCl electrode. All of the tests were conducted in triplicate, and the mean values are presented here.

3. RESULTS AND DISCUSSION

3.1 Morphological characteristics of the nanostructured MnO_2

The FE-SEM images (Figure 1) show the evolution of the nanostructured MnO_2 samples prepared using different dwell times (2 h to 18 h with a step size of 2 h). There was a strong correlation between the dwell time and the resulting morphology of the nanostructured MnO_2 samples. All of the prepared MnO_2 samples appeared to consist of nanostructured flowers and/or nanostructured rods.

For Sample I, which was prepared using a dwell time of 2 h, only nanoflowers were observed during the FE-SEM analysis (Figures 1A, 2A). The corresponding selected-area electron diffraction (SAED) analysis showed the initiation of nucleation of nanocrystalline particles (Figure 2A inset). However, the lattice fringes did not clearly evolve after a dwell time of 2 h. The HR-TEM images presented the polycrystalline pattern of typical microspheres, and the darker/lighter contrast confirmed the core-corona structure of the spheres (Figure 2B). Subsequently increasing the dwell time from 2 to 4, 6, 8, and 10 h yielded corresponding changes in the nanoarchitecture, with a few rods in addition to nanoflower structures (Figures 1B-E), and the ratio of nanorods to nanoflowers in the samples increased with increasing dwell time. Additionally, a tube-like structure was observed in Sample VI (dwell time of 12 h), as verified by the magnified image in the insets of Figures 1F and 2C. The formation of well-developed crystals was shown by the SAED analysis and confirmed by the HR-TEM observation.

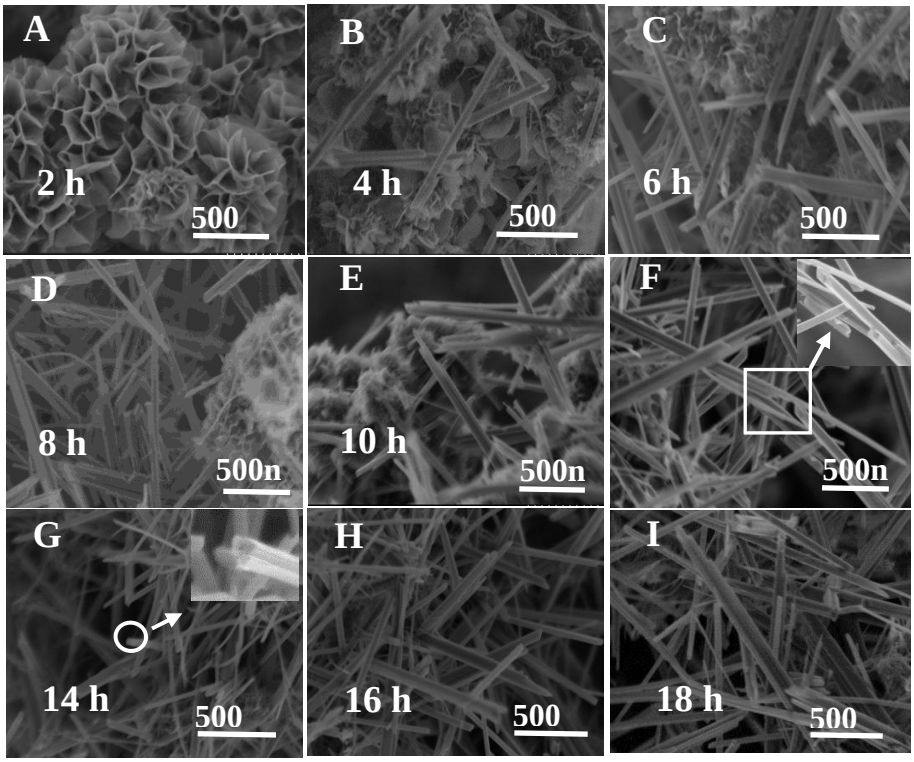

Figure 1. SEM images of MnO_2 prepared using different hydrothermal dwell times

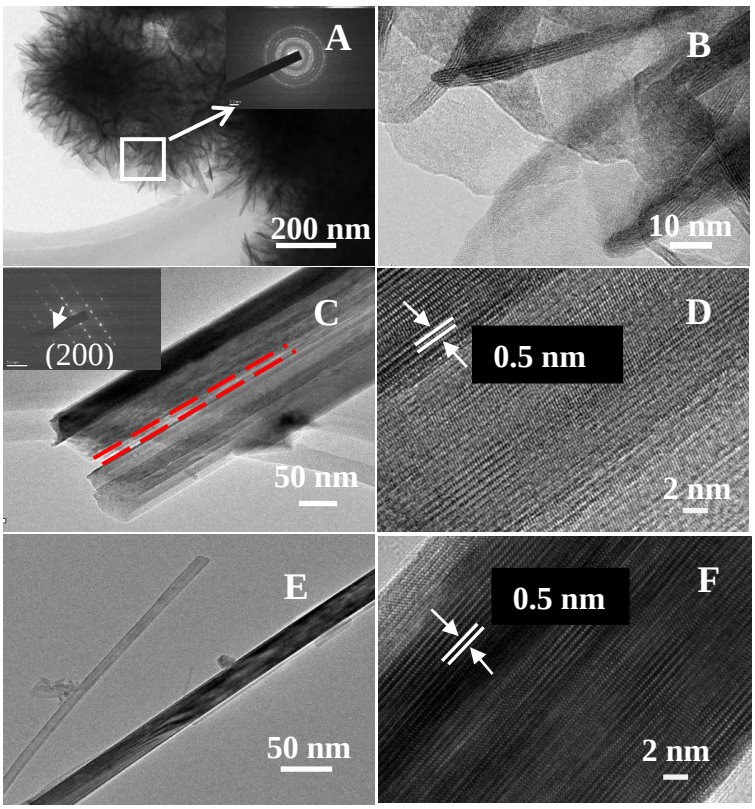

Figure 2. TEM (A, C, and E) and HR-TEM (B, D, and F) images of MnO_2 prepared using dwell times of 2 h, 12 h and 18 h. The insets of A and C show the corresponding SEAD patterns taken from one individual nanostructure.

The morphology of the prepared materials transformed into nanotube with a smooth surface (Figure 2C). An average *d* spacing of approximately 0.5 nm was observed in the lattice-resolved HR-TEM image (Figure 2D), consistent with the spacing between the (200) planes [26]. After dwell times of 14, 16 and 18 h (Samples VII, VIII, and IX), nanoflowers and nanotubes was no longer observed (Figures 1G-I). The magnified image in the inset of Figure 1G shows that the structure of Sample VII had a solid square end with the diameter of the nanorods being smaller compared to those of Sample VI. However, the nanorods retained a smooth surface (Figs. 2E, 2F) and an average *d* spacing of 0.5 nm in Sample VII, consistent with recent findings [27]. Together, the above results suggest that there is a strong correlation between the dwell time and the crystallinity of nanostructured MnO_2 with respect to the surface area.

The BET surface area of Sample I (dwell time of 2 h) was only 65.6 m^2/g (Table 1). As the dwell time was increased to 18 h in steps of 2 h, the BET surface area of the prepared samples first increased and then decreased, with the peak value of 160.2 m^2/g observed in Sample VI (dwell time of 12 h; Table 1). As the dwell time was increased from 2 to 12 h, the nanoflower structures changed into a smaller structure of nanorods and occasionally nanotubes (at 12 h only), accounting for the increased BET surface area; with a further increase in the dwell time from 14 to 18 h, the nanotubes collapsed, and the BET surface area subsequently decreased.

Table 1. The structures and surface areas of nanostructured MnO_2 prepared hydrothermally at 140°C using different dwell times.

Sample	Dwell time (h)	Structure	Surface area (m^2/g)
I	2	Nanoplates	65.7
II	4	Nanoplates and nanorods	101.8
III	6	Nanoplates and nanorods	112.0
IV	8	Nanoplates and nanorods	111.9
V	10	Nanoplates and nanorods	137.9
VI	12	Nanorods and nanotubes	160.2
VII	14	Nanorods	152.7
VIII	16	Nanorods	144.0
IX	18	Nanorods	125.1

3.2 Structural characteristics of nanostructured MnO_2

The XRD patterns show the crystal phases of the MnO_2 samples prepared using different dwell times (Figure 3). The presence of a broad peak implied that the prepared material was essentially a mixture of amorphous and nanocrystalline phases. There was an increasing trend in the crystallinity of the material as the dwell time increased from 2 to 18 h, as indicated by the appearance of sharper peaks.

Sample I (dwell time of 2 h) presented six diffraction peaks at 2θ=approximately 13°, 18°, 26°, 38°, 49°, and 67°, which are indexed to (110), (020), (220), (211), (141), and (541), respectively, with

a tetragonal unit cell with lattice parameters of a=b=9.82 Å and c=2.85 Å, which bear a close resemblance to those of α-MnO_2 (ICDD-JCPDS No. 02-0227). By comparison, Sample II (dwell time of 4 h) had five new peaks at 2θ=approximately 28°, 37°, 42°, 57°, and 59°, which are indexed to (110), (011), (111), (121), and (220), respectively, with a tetragonal unit cell with lattice parameters of a=b=4.39 Å and c=2.87 Å, which bear a close resemblance to those of β-MnO_2 (ICDD-JCPDS No. 24-6888). These results indicate that Sample II contained both α- and β-MnO_2.

For Samples II to IX, there was no remarkable decrease or increase in the number of peaks, indicating the coexistence of α- and β- MnO_2, and there were no obvious changes in the crystalline state of the prepared samples. However, the peaks at 28°, 37°, 42° and 59° became stronger and narrower, suggesting that the crystal of β-MnO_2 in the samples became integrity, crystal structure tend to be more orderly, and crystalline properties tend to be better. According to Zhang's report [18], β-MnO_2 appeared to possess the highest catalytic activity because of its larger BET surface area and higher average oxidation state compared to α- and γ- MnO_2. Therefore, the highest BET surface area of 160.2 m^2/g for Sample VI (Table 1) could be attributed to it possessing the highest content of β- MnO_2 compared with the other samples.

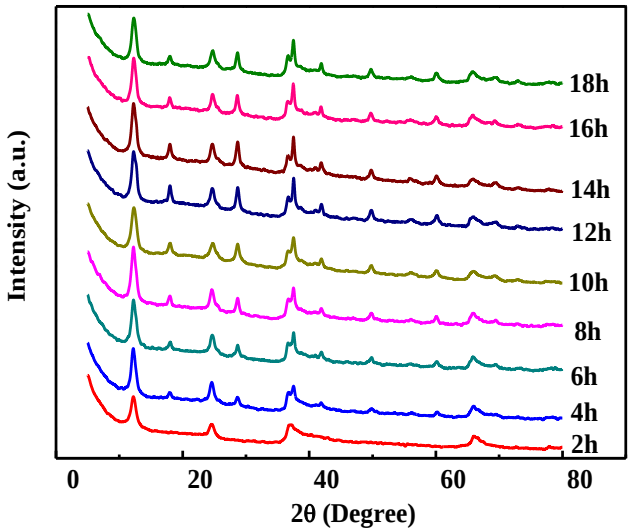

Figure 3. XRD patterns of MnO_2 synthesized hydrothermally at 140℃ using different dwell times

3.3 Electrocatalytic ORR activity of nanostructured MnO_2

The hydrothermally synthesized MnO_2 nanostructures presented a reduction peak (–0.5 to –0.2 V) in the aerobic environment bubbled with O_2 but not in the anaerobic environment bubbled with N_2 (Figure 4). This observation indicates that the peak was attributed to the catalyzed ORR process. The analysis of the electrocatalytic ORR activities of Samples I to IX showed that as the dwell time increased from 2 to 12 h, the ORR peak current correspondingly increased. However, as the dwell time was further increased to 14, 16 and 18 h, a decreasing trend was observed in the ORR peak current.

Such an increase-to-decrease variation tendency in the electrochemical ORR activity was consistent with that in the BET surface area of the prepared samples (Table 1).

To clearly present the results, the CV curves of Samples II, IV, VI, and VIII (dwell times of 4, 8, 12, and 16 h, respectively) are presented in Figure 4. Four peak potentials appeared at approximately –0.433, –0.385, –0.308, and –0.363 V, corresponding to the four samples. Remarkably, Sample VI exhibited a more positive electrochemical ORR activity than the other as-prepared samples and the nanotubes synthesized by Xiao [26] (which had a peak appearing at approximately -0.319 V), which was primarily due to this sample possessing the highest content of β-MnO_2. Because the larger interlayer spacing (0.7 nm) in β-MnO_2 enables the adsorption of more O_2 molecules, electron transfer is facilitated through the film, and the ORR over-potential is decreased [18]. In addition, nanoscale MnO_2 with a porous structure might shorten the solid-state ion transport distances and provide a continuous pathway for the rapid diffusion of electrolytes, thereby improving the electrochemical performance of the electrode materials [28].

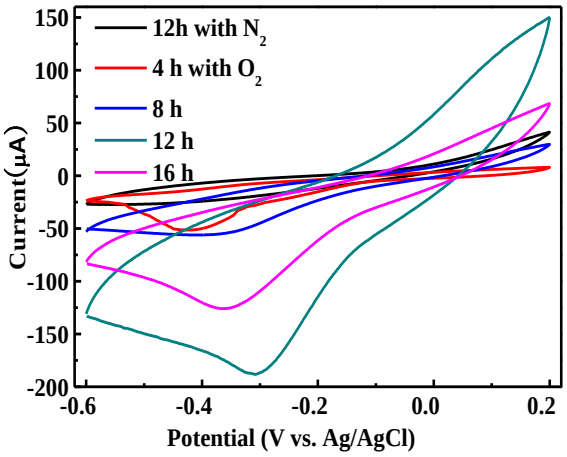

Figure 4. Cyclic voltammograms of MnO_2 for ORR at a scan rate of 100 mV/s in 0.l M KOH.

To obtain further insights into the oxygen reduction kinetics of the samples, RDE measurements were performed. The onset potential for Sample VI was –0.18 V vs. Ag/AgCl, and the values for Samples II, IV, VIII, and Pt/C were –0.27, –0.22, –0.2, and –0.15 V vs. Ag/AgCl, respectively (Figure 5A). At –0.8 V, Samples II, IV, VI, VIII and Pt/C yielded ORR current densities of 1.13, 1.41, 2.82, 2.13, and 5.02 mA/cm^2, respectively. The positive shift of the onset potential and the enhancement in the reduction current for the ORR on the Sample VI electrode clearly indicates that Sample VI possesses ideal catalytic activities. The ORR performance of the Sample VI catalyst in the diffusion-limited and kinetically limited regions was evaluated using Koutecky-Levich (K-L) plots, which are also shown in Figure 5. The K-L plots from the Sample VI electrode exhibited a linear relationship between 1/j and $\omega^{-1/2}$ from - 0.4 V to - 0.475 V, which can be further investigated using the K-L equations [29].

$$\frac{1}{i}=\frac{1}{i_k}+\frac{1}{i_l}=\frac{1}{i_k}+\frac{1}{\left(B\omega^{\frac{1}{2}}\right)} \quad (1)$$

$$i_l=0.2nFD_0^{\frac{2}{3}}\nu^{-\frac{1}{6}}C_0\omega^{\frac{1}{2}} \quad (2)$$

$$i_k=nFkC_0 \quad (3)$$

where i_k is the kinetic current density, i_l is the diffusion-limiting current density, ω is the rotation rate, F is the Faraday constant (96485 C/mol), D_0 is the diffusion coefficient, ν is the kinematic viscosity of the electrolyte, C_0 is the concentration of O_2 in the electrolyte, n is the number of electrons, and k is the electron-transfer rate constant. In the case of a 0.1 M KOH electrolyte at 298 K, D_0 is 1.86×10^{-5} cm^2 s^{-1}, ν is 0.01008 cm^2 s^{-1}, and C_0 is 1.2 mM for saturated O_2. By linear fitting the K-L plots of i^{-1} vs. $\omega^{-0.5}$, the n values for the ORR can be obtained quantitatively [30]. According to Figure 5B, the average n value for Sample VI was between 3.61 and 3.80, indicating that Sample VI follows an electron-transfer pathway that involves nearly four electrons and exhibits excellent ORR activity.

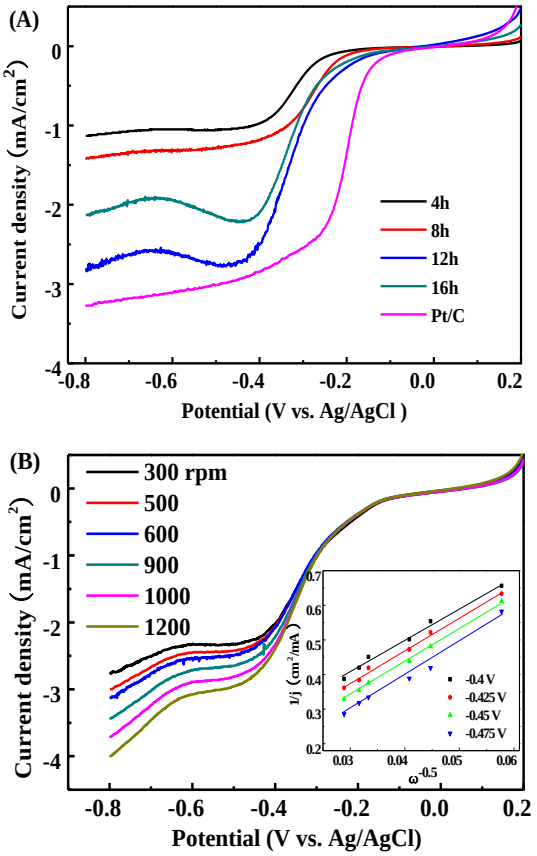

Figure 5. ORR voltammograms of MnO_2 prepared using dwell times of 4 h, 8 h, 12 h, 16 h and of Pt/C (A), rotating-disk voltammograms of the MnO_2 prepared using a dwell time of 12 h in O_2-saturated 0.1 M KOH aqueous electrolyte (B). The inset figure shows the corresponding Koutecky-Levich plot (1/i *vs.* $\omega^{1/2}$)

3.4 Possible mechanism for the formation of nanostructured MnO_2 under hydrothermal conditions

With Mn^{2+} and MnO_4^- as Mn sources, α- and β-MnO_2 nanoflowers/nanorods/nanotubes can be obtained via hydrothermal synthesis. The overall reaction for the primary reagents, $KMnO_4$ and $MnSO_4$, is given in the following equation:

$$2KMnO_4 + 3\ MnSO_4 + 2H_2O \longrightarrow 5\ MnO_2 + K_2SO_4 + 2H_2SO_4$$

SEM images (Figure 1) and XRD patterns (Figure 3) show the phases of the intermediate products at different stages of the hydrothermal synthesis. After a hydrothermal dwell time of 2 h, spherical MnO_2 nanoflowers were obtained in Sample I; the "Ostwald ripening process" can be used to explain the formation of the spherical MnO_2 nanoflowers. During the reaction procedure, a large number of nuclei are formed in a short time and aggregate continuously to form a sphere with a solid core [28].

The number of nanorods in the prepared material increased as the dwell time was further increased (from 4 to 10 h), with the nanoflowers disappearing in Sample VI (dwell time of 12 h). This behavior is reasonable because layered-nanoflower structured MnO_2 is a metastable phase for the MnO_2 crystal form, and the lamellar nanosheets tend to curl and collapse with increasing temperature and dwell time [31]. Additionally, in a $KMnO_4/MnSO_4$ reaction system, where there exists a moderate amount of K^+, the layered structure will initially collapse into a 2×2 tunnel structure and then into a 1×1 structure of β-MnO_2, which is characteristic of the rolling-cum-phase transformation mechanism [29].

Furthermore, nanotubes were observed in Sample VI (dwell time of 12 h), each of which had a square open end (Figure 1F inset). This structure was observed because sufficient MnO_2 molecules could not be provided for the growth of rod-like crystals as the reaction continued, leading to undersaturation in the central part of the growing regions of the rod-like nanoparticles [30]. Then, the nanorods were affected by "dissolution or etching" from both ends inward along the long axis to form nanotubes [26, 27, 32]. That is, the formation of the nanotubes can be described as the "dissolution-recrystallization" of each nanorod from both ends inward along the long axis until the formation of hollow tubes. A similar mechanism of nucleation-dissolution-anisotropic growth-recrystallization has been proposed by Zheng [33], Jia [34], and others. The proposed mechanism awaits confirmation by further studies.

In Samples VII to IX (dwell times of 14 to 18 h), the tube-like structure was no longer observed, and only smaller-sized nanorods were obtained. It is possible that the tube-like nanostructure of MnO_2 collapsed before growing into nanorods during the phase transformation due to the insufficient number of cations, and as the dwell time was increased, an adequate number of MnO_2 molecules were formed, thus leading the rod-like crystal form to grow again [32].

3.5 Application of nanostructured MnO_2 to MFCs

Hydrothermally synthesized MnO_2 nanostructures are often used in batteries and pseudocapacitors [24, 31]. However, their application in MFCs and further comparative analysis of their performance are rarely reported. Therefore, we investigated the catalytic properties of

hydrothermally synthesized MnO_2 nanostructures as cathode catalysts in MFCs. The performance of MFCs with Samples I to IX as the cathode catalysts (MFC-I to MFC-IX, respectively) was assessed by monitoring the cell output, the anode and cathode polarization, and the power density (Figure 6).

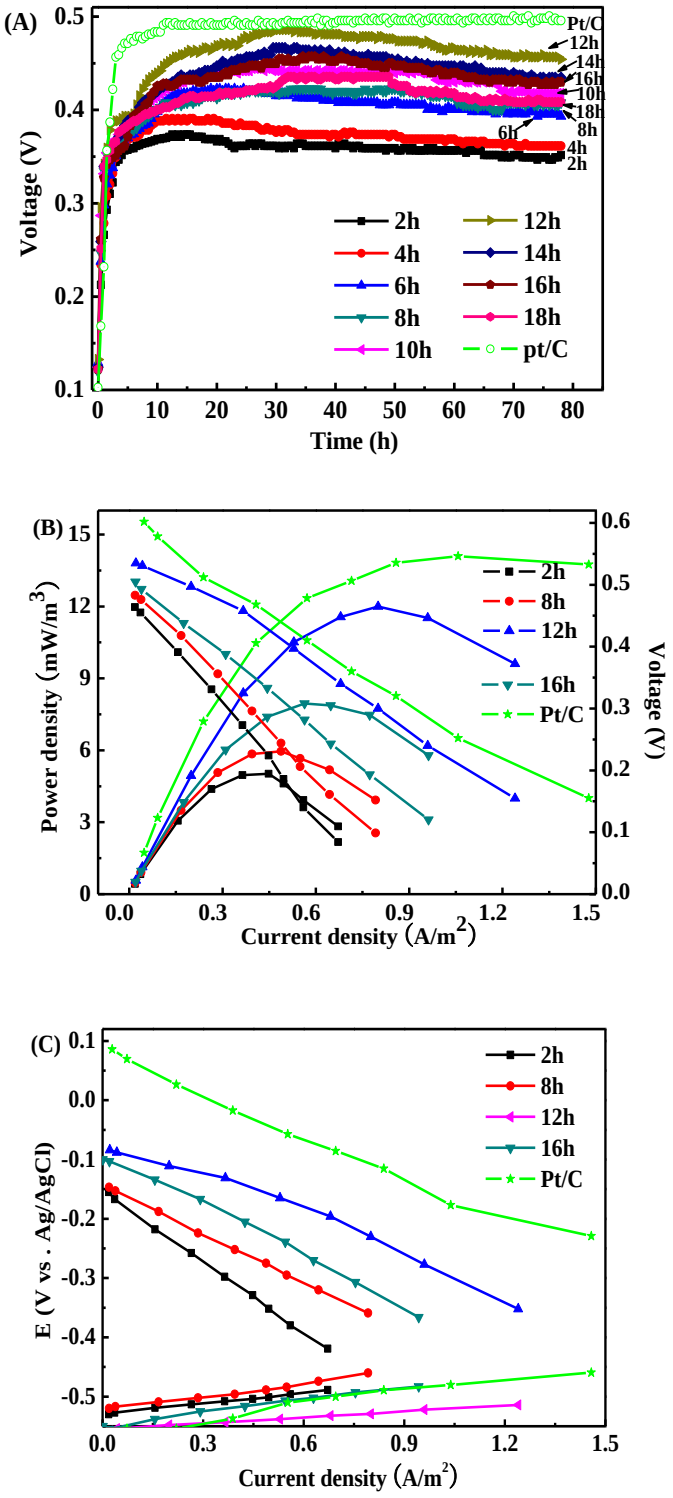

Figure 6. Performance of MFCs equipped with nanostructured MnO_2 and Pt/C. MnO_2 was prepared via hydrothermal syntheses using different dwell times

As the dwell time used during preparation of the catalyst was increased (from 2 h to 18 h), the maximum stable voltage of the MFCs continuously increased from a minimum of 0.37 V (sample I, 2 h) to a maximum of 0.48 V (sample VI, 12 h), followed by a decrease to 0.43 V (sample IX, 18 h, Figure 6A). Sample VI exhibited the best catalytic activity, potentially due to its high content of β-MnO_2, which is characterized by its characteristic peaks and its more effective electrocatalytic properties than the other samples [35]. The variation tendency in the MFC power density was consistent with that of a stable voltage (Figure 6B and Table 2). The power density produced by MFC-VI (11.6 W/m^3 or 240 mW/m^2) was 45-130% higher than those of MFC-II (5.0 W/m^3), MFC-IV (6.0 W/m^3) and MFC-VIII (8.0 W/m^3), comparable to that of MFC-O (Pt/C, 14.1 W/m^3) and greater than that of the carbon nanotube-supported β-MnO_2 synthesized by Lu et al. [15]. The anode and cathode polarization curves (Figure 6C) clearly show that the cathode was a limiting factor for these MFC reactors. Taking MFC-VI as an example, as the current density increased from 0.02 to 1.24 A/m^2, the anode potential slightly increased from -0.54 to -0.50 V, and the cathode potential substantially decreased from -0.06 to -0.33 V. The larger driving force with over-potential of 0.27 V required for the cathode compared with 0.04 V required for the anode indicated that the power generation from the MFC was dominated by cathode polarization.

Table 2. Performance of microbial fuel cell reactors based on nanostructured MnO_2 prepared through hydrothermal syntheses using different dwell times.

Microbial fuel cell (dwell time)	Open circuit voltage (V)	Maximum power density (W/m^3)	Maximum current density (A/m^2)
MFC-O(Pt/C)	0.60	14.1	0.88
MFC-I (2 h)	0.47	3.7	0.38
MFC-II (4 h)	0.48	5.0	0.45
MFC-III (6 h)	0.50	5.6	0.47
MFC-IV (8 h)	0.50	6.0	0.49
MFC-V (10 h)	0.52	8.0	0.56
MFC-VI (12 h)	0.54	11.6	0.80
MFC-VII (14 h)	0.52	8.3	0.67
MFC-VIII (16 h)	0.51	8.0	0.56
MFC-IX (18 h)	0.51	7.3	0.54

Moreover, the open-circuit voltage (OCV) of MFC-VI was observed to be the highest among all of the as-prepared samples (~0.54 V) (Table 2). The main factors that influence the OCV include the cell structure, the electrode material, the solution composition and concentration, the temperature, and the electricity interface state. Because no other changes occurred in the MFC systems except in the cathode catalyst, the higher OCV of MFC-VI indicated that Sample VI (dwell time of 12 h) had more positive catalytic properties than the other samples. It is believed that the as-prepared nanotubes present many advantages as electrocatalysts for the ORR. First, the cost of the as-prepared catalyst is

very low. Second, the strategy could be easily scaled up for mass production because the entire process is easy to perform.

4. CONCLUSIONS

In summary, nanoflowers, nanorods and nanotubes were successfully fabricated using a facile hydrothermal method. The crystal structure of nanostructured MnO_2 exhibited four primary evolutionary stages over time. As the hydrothermal dwell time was increased from 2 h to 18 h in 2 h steps, both the BET surface area and the electrochemical oxygen-reduction activity of the obtained materials first increased and then decreased, and the highest levels were obtained after a dwell time of 12 h. When used as a cathode catalyst in microbial fuel cells, the maximum power density of 11.6 W/m^3 was produced with the material prepared using a dwell time of 12 h (containing nanotubes), and this power density is considerably higher than those obtained with the other samples and comparable to that obtained with Pt/C (14.1 W/m^3). The results of this study demonstrate that nanotubes are ideal crystal structures for MnO_2 and that they offer a good alternative to Pt/C for practical MFC applications.

ACKNOWLEDGEMENT
We gratefully acknowledge financial support from the National 973 project of China (2011CB201501), Projects of International Cooperation and Exchanges NSFC (51161140330), Knowledge Innovation Program of the Chinese Academy of Sciences (NKSCX2-EW-G-1-5), and The Program of Guangdong Province - Chinese Academy of sciences strategic cooperation (2010A090100035).

References

1. B.E. Logan, *Nat. Reviews Microbiol.*, 7 (2009) 375
2. Y. Ahn and B.E. Logan, *Bioresour. Technol.* 101 (2010) 469
3. G. Antonopoulou, K. Stamatelatou, S. Bebelis and G. Lyberatos, *J.Biochem. Eng.*, 50 (2010) 10
4. E. Martin, O. Savadogo, S. Guiot and B. Tartakovsky, *J.Biochem. Eng.*,51 (2010) 132
5. M. Lu and S.F.Y. Li, *Crit. Rev. Env. Sci. Technol.V.*, 42 (2012) 2504
6. J.K. Jang, T.H. Pham, I.S. Chang, K.H. Kang, H. Moon, K.S. Cho and B.H. Kim, *Process Biochem.*, 39 (2004) 1007
7. I.S. Chang, H. Moon, J.K. Jang and B.H. Kim, *Biosens. Bioelectron.*, 20 (2005) 1856
8. Y.C. Chen, Y.K. Hsu, Y.G. Lin, Y.K. Lin, Y.Y. Horng, L.C. Chen and K.H. Chen, *Electrochim. Acta.*, 56 (2011) 7124
9. L. Zhang, C. Liu, L. Zhuang, W. Li, S. Zhou and J. Zhang, *Biosens. Bioelectron.*, 24 (2009) 2825.
10. R.S. Kalubarme, M.-S. Cho, K.-S. Yun, T.-S. Kim and C.-J. Park, *Nanotechnol.*, 22 (2011) 395
11. X.W. Liu, X.F. Sun, Y.X. Huang, G.P. Sheng, K. Zhou, R.J. Zeng, F. Dong, S.G. Wang, A.W. Xu and Z.H. Tong, *Water res.*, 44 (2010) 5298
12. M. Mahmoud, T.A. Gad-Allah, K. El-Khatib and F. El-Gohary, *Bioresour. Technol.*, 102 (2011) 10459
13. X. Li, B. Hu, S. Suib, Y. Lei and B. Li, *J. Power Sources*, 195 (2010) 2586

14. X. Li, B. Hu, S. Suib, Y. Lei, B. Li and *J.Biochem. Eng.*, 54 (2011) 10
15. T.T. Truong, Y. Liu, Y. Ren, L. Trahey and Y. Sun, *ACS nano*, 6 (2012) 8067.
16. H. R.Yuan, L. F.Deng, T. Lu and Y. Chen, *The Scienti. World*, 2014(2014),1
17. Y. Hou, Y. Cheng, T. Hobson and J. Liu, *Nano lett.*, 10 (2010) 2727.
18. I. Roche, K. Katuri and K. Scott, *J. Appl. Electrochem.*, 40 (2010) 13.
19. Y. Zhang, Y. Hu, S. Li, J. Sun and B. Hou, *J. Power Sources*, 196 (2011) 9284
20. Y. Chen, Z. Lv, J. Xu, D. Peng, Y. Liu, J. Chen, X. Sun, C. Feng and C. Wei, *J. Power Sources*, 201 (2012) 136.
21. M. Lu, S. Kharkwal, H.Y. Ng and S.F.Y. Li, *Biosens. Bioelectron.*, 26 (2011) 4728.
22. G. Gnana kumar, C.J. Kirubaharan, S. Udhayakumar, C. Karthikeyan and K.S. Nahm, *Ind. Eng. Chem. Res.*, 43(2013)461.
23. G. Gnana kumar, C.J. Kirubaharan, S. Udhayakumar, K. Ramachandran, C. Karthikeyan, R. Renganathan and K.S. Nahm, *ACS Sus. Chem. Eng.*, 53(2014)528.
24. V. Subramanian, H. Zhu and B. Wei, *J.Power Sources*, 159 (2006) 361
25. L.F. Deng, F.B. Li, S.G. Zhou, D.Y. Huang and J. R. Ni, *Chin.Sci. Bull.*, 55 (2010) 99.
26. W. Xiao, D. Wang, X.W. Lou and *J. Phys. Chem. C*, 114 (2009) 1694.
27. J. Luo, H. Zhu, H. Fan, J. Liang, H. Shi, G. Rao, J. Li, Z. Du and Z. Shen, *J. Phys. Chem. C*, 112 (2008) 12594.
28. X. Zhang, X. Sun, H. Zhang, D. Zhang and Y. Ma, *Electrochim. Acta*, 87 (2013) 637.
29. X. Wang, Y. Li, *J. Chem. Euro.*, 9 (2003) 300.
30. Q. Tang, Z. Liu, S. Li, S. Zhang, X. Liu and Y. Qian, *J.Cryst. Growth*, 259 (2003) 208.
31. X. Zhang, P. Yu, D. Wang and Y. Ma, *J. Nanosci. Nanotechnol.*, 10 (2010) 898.
32. M. Chen, Y. Xie, J. Lu, Y. Xiong, S. Zhang, Y. Qian and X. Liu, *J. Mater. Chem.*, 12 (2002) 748.
33. D. Zheng, S. Sun, W. Fan, H. Yu, C. Fan, G. Cao, Z. Yin and X. Song, *J. Phys. Chem. B*, 109 (2005) 16439.
34. C.J. Jia, L.D. Sun, Z.G. Yan, L.P. You, F. Luo, X.D. Han, Y.C. Pang, Z. Zhang and C.H. Yan, *Angew. Chem. Int. Ed.*, 117 (2005) 4402.
35. S. Donne, A. Hollenkamp and B. Jones, *J. Power Sources*, 195 (2010) 367.